Coupling between the Atlantic cold tongue and the West African monsoon in boreal spring and summer

Guy Caniaux,[1] Hervé Giordani,[1] Jean-Luc Redelsperger,[1] Françoise Guichard,[1] Erica Key,[2] and Malick Wade[1,3]

Received 3 August 2010; revised 15 November 2010; accepted 5 January 2011; published 5 April 2011.

[1] The formation of the Atlantic cold tongue (ACT) is the dominant seasonal sea surface temperature signal in the eastern equatorial Atlantic (EEA). A comprehensive analysis of variability in its spatial extent, temperature, and onset is presented. Then, the physical mechanisms which initiate ACT onset, as well as the feedbacks from the ACT to the maritime boundary layer, and how the ACT influences the onset of the West African monsoon (WAM) are discussed. We argue that in the EEA, the air-sea coupling between the ACT and WAM occurs in two phases. From March to mid-June, the ACT results from the intensification of the southeastern trades associated with the St. Helena anticyclone. Steering of surface winds by the basin shape of the EEA imparts optimal wind stress for generating the maximum upwelling south of the equator. During the second phase (mid-June–August), wind speeds north of the equator increase as a result of the northward progression of the intensifying trades and as a result of significant surface heat flux gradients produced by the differential cooling between the ACT and the tropical waters circulating in the Gulf of Guinea (GG). It is anticipated that the atmospheric divergence induced at low levels north of the equator reduces convection over the GG and that increased northward winds shift convection over land. Correlations between the ACT and the WAM onset dates over the last 26 years (1982–2007) measure as much as 0.8. This suggests that the ACT plays a key role in the WAM onset.

Citation: Caniaux, G., H. Giordani, J.-L. Redelsperger, F. Guichard, E. Key, and M. Wade (2011), Coupling between the Atlantic cold tongue and the West African monsoon in boreal spring and summer, *J. Geophys. Res.*, *116*, C04003, doi:10.1029/2010JC006570.

1. Introduction

[2] The eastern equatorial Atlantic (EEA) is the region of the Atlantic basin where the seasonal climatic cycle is most accentuated [*Wauthy*, 1983]. Indicators of this strong seasonal cycle include (1) large seasonal variations in sea surface temperatures (SSTs) that can reach 5 to 7°C in the Atlantic cold tongue (ACT) [*Weingartner and Weisberg*, 1991] and 4°C in coastal upwelling areas [*Hardman-Mountford and McGlade*, 2003]; (2) intensifying winds that escalate with sustained southeastern trades in boreal spring and summer, over the EEA, the meridional component of the winds increases most during this period [*Hastenrath and Lamb*, 1978]; and (3) displacement of the ITCZ, located between the equator and 5°N in boreal winter and early spring, it migrates poleward to 10°N in summer over the African continent [*Waliser and Gautier*, 1993]. During this seasonal march, an abrupt northward shift is noted in the longitudinally averaged rainfall [*Le Barbé et al.*, 2002] and outgoing longwave radiation (OLR) in June–July [*Sultan and Janicot*, 2000]. This shift is referred to as the West African monsoon (WAM) onset [*Sultan and Janicot*, 2003].

[3] The relationship between winds, SSTs and WAM in the tropical Atlantic is generally viewed as strongly influenced by the seasonal intensification of the southeasterlies, which, after crossing the equator, meet the northeastern trades of the northern hemisphere. The resulting convergence feeds atmospheric convection in the ITCZ. SST cooling, regulated by the upwelling that is driven by the Ekman divergence on the equator [*Li and Philander*, 1997], results in decreased atmospheric convection in the Gulf of Guinea (GG) [*Mitchell and Wallace*, 1992] while the warmest SSTs migrate and settle in the central-north equatorial Atlantic. As warm SSTs favor convection through their effect on moist static energy [*Philander et al.*, 1984], the northward migration of the ITCZ is coincident with the northwestward migration of warm SSTs.

[4] The ACT cooling has been attributed to various physical processes: advection of cold water upwelled along the African coast [*Hastenrath and Lamb*, 1978], vertical advection of underlaying cold water [*Voituriez*, 1981], and western deepening/eastern shallowing of the thermocline across the

[1]CNRM-GAME, Météo-France, CNRS, URA 1357, Toulouse, France.
[2]LDEO, Columbia University, Palisades, New York, USA.
[3]LPAOSF, Dakar, Senegal.

0148-0227/11/2010JC006570

basin [*Adamec and O'Brien*, 1978; *Busalacchi and Picaut*, 1983]. These studies highlight different processes, but they all consider that the ACT appearance is in phase with the intensification of the southeastern trades, and that this cooling is a passive response of the ocean to their seasonal intensification.

[5] However, there are instances in the recent literature which link the formation of the ACT to a cooling that influences the northward migration of the WAM and modulates the intensity of related rainfall. *Vizy and Cook* [2002] analyzed the influence of Gulf of Guinea SST anomalies (SSTAs) relative to climatology on the WAM and could simulate the well-established fact that precipitation decreases over the Sahel and increases along the Guinean coast in response to warm SSTAs in the GG. They found that the increase in rainfall along the Guinean coast is associated with an increase in lower tropospheric water vapor content due to enhanced evaporation over the warm SSTAs and a decrease in rainfall over the southern Sahel that is associated with enhanced subsidence in the lower troposphere as the monsoon circulation is shifted equatorward. This proves that, at least at interannual time scales, the WAM and ACT interact together.

[6] *Gu and Adler* [2004] considered that rainfall of the WAM is concentrated in two main regions: one over the GG with convection and rainfall in April–June and the other along latitudes of about 10°N over the interior of West Africa with rain in July and later summer, both being separated spatio-temporally by the monsoon jump. They argued that these two main regions are dominated by different processes: over the interior of West Africa, rainfall results from various dynamical components, while over the GG, convection would be primarily modulated by the seasonal thermal forcing from the ocean and by the leading SST-related meridional gradient.

[7] In order to test the importance of the ACT on the WAM, *Okumura and Xie* [2004] conducted two ensemble experiments with an AGCM: one with prescribed SSTs with their full climatological seasonal cycle and the other with equatorial Atlantic SSTs held constant during boreal spring and summer. The difference between the two simulations indicates an increase in the northward gradients of temperature and an acceleration of the southerly winds over the GG when the ACT is present. The intensity of this wind increase suggests that the ACT contributes to the WAM onset in the GG and to the northward advance of rainbands on West Africa.

[8] *Hagos and Cook* [2009] studied the interactions between the WAM and the eastern tropical Atlantic Ocean with a coupled model. Between April and July, the monsoon season is accompanied by an increase of the meridional component of the wind stress over the GG by 50%, in agreement with satellite wind stress accelerations, although the wind stress is underestimated by 25%, while the ACT SSTs are warmer by up to 3°K. Their study underscores the current limitation of coupled models to accurately simulate the three-way interactions among Atlantic SSTs, low-level winds and precipitation [*Richter and Xie*, 2008]. However, their study clearly states that SST seasonal cycle over the eastern equatorial Atlantic determines both the enhancement of surface wind stress and the availability of moisture for transport into the continent.

[9] These studies have established a link between the ACT and convection over West Africa. However, the processes that couple the WAM-ACT complex, the timing of this coupling and the leading pertinent parameters of this coupling have not been clearly documented in the literature. In particular, much of the results obtained rely on large-scale modeling. In the present study, we adopt a more directly observationally based approach. An ensemble of data sets is used to further explore their relationship, and to identify the factors causing and affecting the ACT as well as coupling between the ACT and the WAM. First, the ACT is defined from appropriate indexes characterizing its surface area, intensity and dates of formation/dissipation. This analysis of the interannual variability of the ACT covers the last 27 years. To our knowledge, this has not been done before. Second, in order to explain its genesis, a simple model is used to relate the SST and wind stress fields. All these aspects are developed in section 2. The next question is whether the presence of the ACT and SST-related surface heat fluxes lead to a response in the surface wind field, able to modify the low-level monsoon flow. This question is treated in section 3, which includes discussion of the detailed links between SST, surface heat fluxes, SST gradients, flux gradients and their relationship with surface winds. Section 3 also presents some statistical link between the ACT and WAM onset dates. In the conclusion (section 4), a conceptual model is proposed of how the coupling between the ACT and the WAM operates and this model is discussed with previous existing models of the WAM-ACT complex.

2. The Atlantic Cold Tongue

2.1. Definition of the Atlantic Cold Tongue

[10] The ACT is the most pronounced signal of the annual cycle in the equatorial Atlantic basin [*Merle et al.*, 1980]. Despite a decrease in SST over most of the EEA during boreal spring and summer, cooling is greatest south of the equator between the African coast and 20°W. SSTs vary between 27°C and 29°C in the warm season and below 22°C in the ACT during the cold season.

[11] In this paper, the ACT has a surface area (S_{ACT}) and intensity defined by an SST index (TI_{ACT}) computed as

$$S_{ACT} = \int_{A(x)} H_e(25^\circ\mathrm{C} - SST(x))dA \tag{1}$$

$$TI_{ACT} = \frac{\int_{A(x)} (25^\circ\mathrm{C} - SST(\mathrm{x}))H_e(25^\circ\mathrm{C} - SST(x))dA}{S_{ACT}}, \tag{2}$$

where H_e is the Heaviside function ($H_e = 1$ when SST < 25°C and 0 otherwise). The SST index expresses the intensity of the cooling in the ACT and is defined point by point by subtracting the SST for each grid point from a SST of 25°C (so that SSTs below 25°C imply a positive index) inside the domain A, 30°W–12°E and 5°S–5°N. The 25°C threshold has been chosen because it is lower than the average SST reached in June in the EEA [*Bakun*, 1978; *Picaut*, 1983]. The domain includes the area of maximum annual SST variability observed in the EEA [*Picaut*, 1983]. The southern boundary of the domain is set to 5°S, because southward of this latitude, 25°C water can occur as a result of southern hemispheric

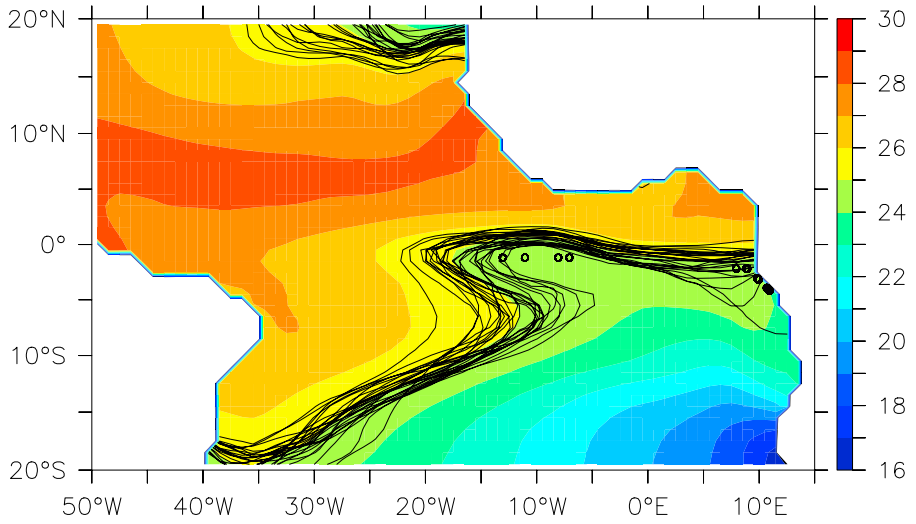

Figure 1. Mean extension of the 25°C isotherm during 1982–2008 as determined from *Reynolds et al.*'s [2007] sea surface temperature analysis (black lines). In color is the 27 year mean SST at the time the Atlantic cold tongue reaches its yearly mean extension. Open circles indicate the position where the Atlantic cold tongue first appeared during the 27 years of the series.

cooling during the austral winter season. The northern limit at 5°N excludes the Senegalese upwelling while the westward limit at 30°W is beyond the maximum westward extension of the ACT.

[12] It is also possible to define the ACT onset as the date at which a threshold area is exceeded (after 1 April); it follows that the conclusion of the ACT is the date when its surface area falls below that threshold after 1 September. Based on an ensemble of the individual years, we empirically fixed the surface threshold at 0.40×10^6 km^2. *Reynolds et al.*'s [2007] SSTs are used, as they cover a significant 27 year long period from 1982 to 2008. These fields are daily and operationally produced from satellite and in situ data using an optimum interpolation scheme on a 1/4° grid. After 2002, the analyses include AMSR-E (Advanced Microwave Scanning Radiometer-EOS) satellite data.

2.2. Interannual Variability

[13] Figure 1 summarizes the annual extent of the ACT, its variability over the period 1982–2008 and the position where the ACT starts to form (i.e., a superpixel of 2° of longitude-latitude where the 25°C SST threshold is reached for the first time during the cold season). The classical features of the ACT emerge: (1) the robustness of this Atlantic signal which appears every year in the EEA; (2) its position south of the equator, with a maximum longitudinal extent to almost 20°W; (3) its center, located a few degrees south of the equator in the eastern part of the basin and slightly shifted equatorward east of 5–10°W, a region where surface winds become more zonal and force equatorial upwelling [e.g., *Colin*, 1989; *Li and Philander*, 1997]; and (4) a large interannual variability present in its westward (between 12°W and 22°W) and southwestward extensions. This last point contrasts with the yearly position of its northern equatorial boundary which varies less. The depicted ACT preferentially forms near 10°W and offshore of the African coast (Figure 1), in agreement with *Mazeika* [1968].

[14] Statistics, including the mean (over the 27 years considered) and maximum surface area reached by the ACT, dates when the maximum is reached, temperature index, dates of formation and disappearance and duration of the ACT, are given in Table 1. During the period 1982–2008, the mean surface area of the ACT (averaging over the period when ACT exists) was $0.99 \pm 0.22 \times 10^6$ km^2. A 27 year mean maximum of nearly double this size ($2.56 \pm 0.50 \times 10^6$ km^2, an area nearly one fourth the size of the Sahara) is attained in mid-August with a standard deviation of 2 weeks (Table 1 and Figure 2a). However, considerable variability of the date of maximum extension exists with dates ranging from 18 July to 20 September.

[15] To give an order of magnitude of the interannual variability of the ACT extent, the 27 year series of mean surface area is analyzed (Table 1). Years 1983, 1986, 1991, 1992, and 2000 can be considered as the most extensive ACTs of the last recent years with mean surface areas ranging from 1.22×10^6 km^2 to 1.49×10^6 km^2 and more than 1 standard deviation above the mean over the 27 years. Years 1984, 1987, and 2007, with areas ranging from 0.65×10^6 km^2 to 0.76×10^6 km^2, were the smallest in size. The difference between the most extreme years is (O)10^6 km^2, i.e., almost the 27 year mean. This underscores the important interannual variability of the ACT surface area.

[16] During the formation period, cooling is the most intense in May and June, slowing in July–August (Figure 2b). The seasonal evolution of the ACT cooling is asymmetric with a short period of formation (3.5 months) followed by a longer (nearly 5 months) period of warming. Note also that the temperature index (Figure 2b) reaches the maximum value about half month earlier than the surface area index (Figure 2a). The average temperature index of the ACT for the period 1982–2008 (Table 1) is 0.61 ± 0.12°C, ranging from 0.36°C in 1984 to 0.80°C in 1992. The coldest years (index greater than the 27 year mean plus 1 standard deviation) are listed in decreasing order: 1992, 1982, 2005, and 2000. The warmest temperature index exceeded three times

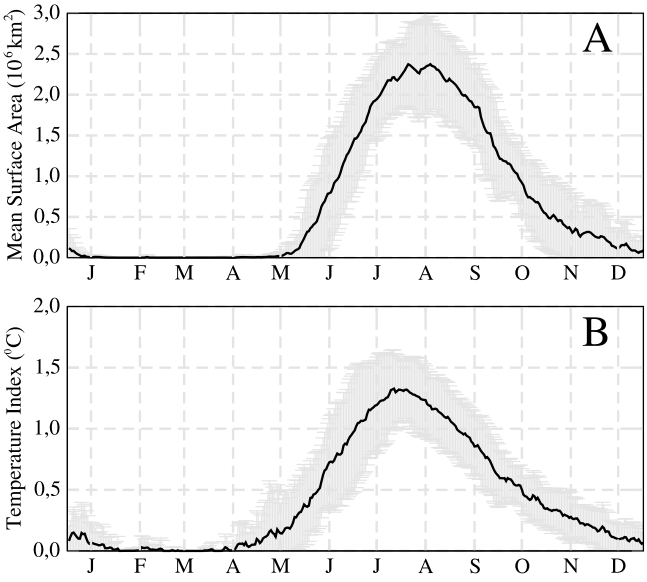

Figure 2. Seasonal evolution of 27 year mean (a) surface area (10^6 km^2) and (b) temperature index (°C) of the Atlantic cold tongue computed from the *Reynolds et al.* [2007] sea surface temperatures over the period 1982–2008. Bars represent 1 standard deviation. Each month is centered around the 15th of that month.

the average minus 1 standard deviation in 1984, 1987, and 1988. Their occurrence confirms that warm events exist in the ACT.

[17] Using the criteria defined in section 2.1, the 27 year mean date of the ACT formation has been determined to be 11 June with a standard deviation of 12 days (Table 1). During the last 27 years, the formation date varied between 19 May and 4 July, which represents a difference of 47 days between the year of earliest onset (2005) and the latest onset (1995). The mean lifetime of the ACT is 149 ± 28 days, nearly 5 months. Extrema in duration include the longest-lasting ACT in 1982 (206 days), which is more than double the briefest ACT, which occurred in 1988 (107 days, Table 1).

[18] From Figure 3, it is apparent that longer-lived events tend to form earlier and to have larger surface area ($r^2 = 0.66$, estimate error = 1.25). It is noted that there is a relatively large spread of the data around the second diagonal of the diagram, indicating that duration and formation dates are not tightly correlated. Moreover, Figure 3 also indicates that an early onset ACT does not automatically imply a longer-lasting ACT (or a particularly cold ACT). For instance, 2005, the earliest year of formation over the last 27 years, can be considered as a quasi-normal year in term of length and extension. This suggests that the factors determining interannual variability of the ACT are numerous and independent of each other.

[19] In conclusion, the ACT can be considered as an area of seasonally cool SSTs, confined to an area south and near the equator, extending from the African coast to ~20°W.

Table 1. Statistics of the Atlantic Cold Tongue for the Last 27 Years, 1982–2008[a]

Year	Mean Surface Area (10^6 km^2)	Maximum Surface Area (10^6 km^2)	Date of Maximum Surface Area	Temperature Index (°C)	Date of Formation	Date of End	Duration (days)
1982	1.17	**3.46**	08/04	**0.79**	06/01	**12/24**	**206**
1983	**1.22**	3.00	08/21	0.72	**05/24**	**11/29**	**189**
1984	*0.65*	*2.00*	08/10	*0.36*	06/15	10/24	131
1985	1.06	2.63	08/27	0.60	06/01	11/07	159
1986	**1.31**	**3.11**	08/18	0.71	06/12	**12/11**	**182**
1987	*0.66*	*1.87*	08/03	*0.43*	06/15	10/27	134
1988	0.79	*2.03*	08/11	*0.44*	*06/29*	10/13	*107*
1989	1.01	2.39	*08/30*	0.63	06/20	11/05	138
1990	0.97	**3.23**	08/13	0.56	06/08	10/15	129
1991	**1.24**	2.55	08/20	0.69	06/23	**12/22**	**182**
1992	**1.49**	**3.55**	08/17	**0.80**	**05/27**	**12/05**	**192**
1993	0.89	2.89	08/06	0.53	06/02	10/18	138
1994	1.05	2.80	08/02	0.72	06/10	11/08	151
1995	0.94	2.60	08/12	0.63	*07/04*	11/01	*120*
1996	0.92	2.51	08/04	0.64	*06/27*	**12/12**	168
1997	1.14	**3.21**	08/12	0.68	**05/26**	10/23	150
1998	0.77	*1.93*	08/17	0.50	*06/24*	10/30	128
1999	0.78	*2.03*	*09/20*	0.50	06/14	10/21	129
2000	**1.40**	**3.13**	*09/02*	**0.74**	06/12	**12/01**	172
2001	1.14	2.83	08/23	0.67	06/07	**12/19**	**195**
2002	1.04	2.15	*09/07*	0.59	06/16	11/09	146
2003	0.90	2.10	07/31	0.49	06/01	10/21	142
2004	0.89	2.10	**07/18**	0.65	06/05	*09/22*	*109*
2005	1.05	2.57	08/16	**0.77**	**05/19**	10/27	161
2006	0.79	2.32	08/19	0.53	06/23	10/24	123
2007	*0.76*	2.24	**07/18**	0.51	06/22	10/22	122
2008	0.77	*1.96*	08/16	0.56	06/21	10/23	124
Mean	0.99	2.56	08/14	0.61	06/11	10/31	149
SD	0.22	0.50	14	0.12	12	25	28

[a]In bold (italic), are values greater (less) than 1 standard deviation, except for the dates of maximum surface area and formation, where bold (italic) are less (greater) than 1 standard deviation. SD, standard deviation. Dates are given in the format mm/dd; read 08/04 as 4 August.

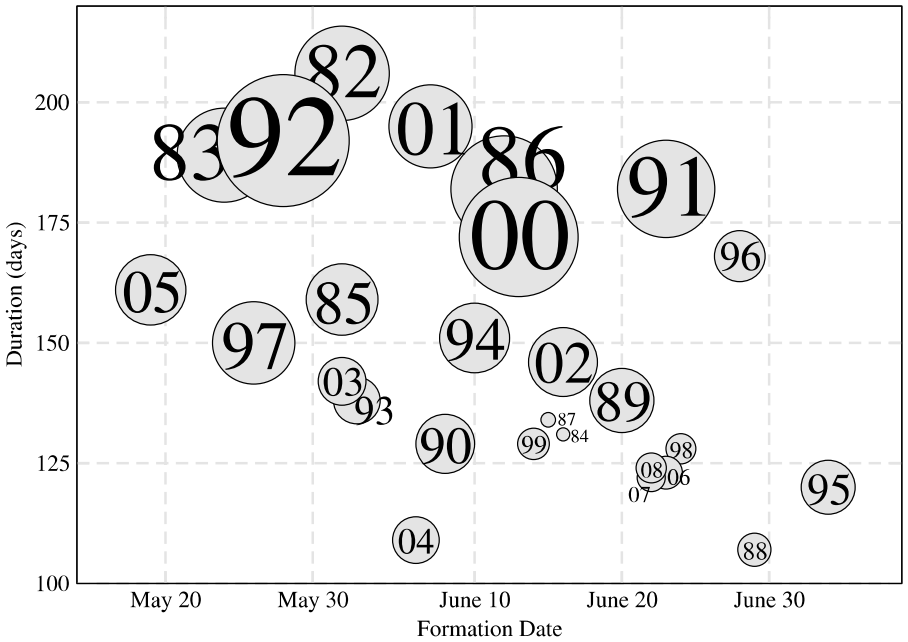

Figure 3. Diagram representing duration (days) versus formation date of the Atlantic cold tongue over the period 1982–2008. The diameter of each circle is proportional to the mean surface area; the larger the circle, the larger the surface area.

Its southern boundary connects with the seasonal cooling of the southern hemisphere SSTs (see Figure 1). Its reappearance every year is remarkable, despite a considerable interannual variability in the date of its appearance/disappearance, duration, cooling intensity and surface area. It is expected that this cold feature, both located in the equatorial waveguide and on the path of the monsoon flow, can affect the low levels of the atmosphere and the monsoon flow itself.

2.3. Formation Mechanisms

[20] Several mechanisms have been proposed to explain upwelling in the EEA. *Picaut* [1983] reviewed the following formation mechanisms: (1) the divergence induced along the equator by the trade winds [*Stommel*, 1960; *Philander*, 1990]; (2) the vertical mixing resulting from the current shear present between the westward South Equatorial Current (SEC) and the eastward Equatorial Undercurrent (EUC) [*Hisard*, 1973; *Voituriez and Herbland*, 1977]; (3) the remote wind forcing in the western equatorial Atlantic which can induce a shallower thermocline in the EEA through excitation of equatorial Kelvin waves [*Adamec and O'Brien*, 1978; *Houghton*, 1989]; and (4) advection of cold water from the southern coastal upwelling areas by the equatorial current system, intensified by meridional winds in the EEA [*Philander and Pacanowski*, 1981a].

[21] Clearly, a single process cannot account alone for the formation of the ACT, which rather results from a combination of mechanisms. The remote wind forcing theory, for instance, plays an important role in ACT formation as a preconditioning phase for initiating shallow mixed layer depths and hence rapid surface cooling in the EEA. As indicated for instance by *Picaut* [1983] or *Colin* [1989], this cooling appears as soon as the zonal component of the wind strengthens in the western part of the basin in early spring. In an observational study, *Mitchell and Wallace* [1992], and in a modeling study, *Li and Philander* [1997] suggested that over the EEA the meridional (southerly) component of the wind can also act as an important driver of the dynamics of the ACT.

[22] Intense current shear between the SEC and EUC is another key process which can induce strong cooling in the upper layers through vertical mixing. In the EEA, the core of the EUC is characterized by velocities up to 1 m s^{-1} near 70 m; but, its core depth is strongly related to the vertical migration of the thermocline [*Kolodziejczyk et al.*, 2009]. When the EUC is near the surface in spring and summer, it favors, in the upper layer, a strong vertical shear with the SEC, the intensity of which is tightly related to the reinforcement of the surface winds [e.g., *Stramma and Schott*, 1999; *Kolodziejczyk et al.*, 2009].

[23] The common feature that unifies all proposed mechanisms is that the formation of the ACT coincides with the intensification of the southeasterly trades in early boreal summer. However, determination and representation of the complex vertical processes active in the ACT during the various stages of its seasonal cycle remains an important, unresolved question. The Ekman theory provides a mechanism able to cool the mixed layer and SSTs, via vertical velocity [e.g., *Okumura and Xie*, 2004; *Hagos and Cook*, 2009]. Hereafter, it is used in a qualitative way to explain the main seasonal and geographical features of the observed cooling. This simplified theory considers an unstratified, spatially homogeneous slab ocean mixed layer at rest forced only by a surface wind stress, and assumes a linear distribution of the momentum flux in the mixed layer. Based on these hypotheses, and keeping a constant adjustment time, the mixed layer response to the surface wind stress can be formulated as a response in terms of vertical velocity.

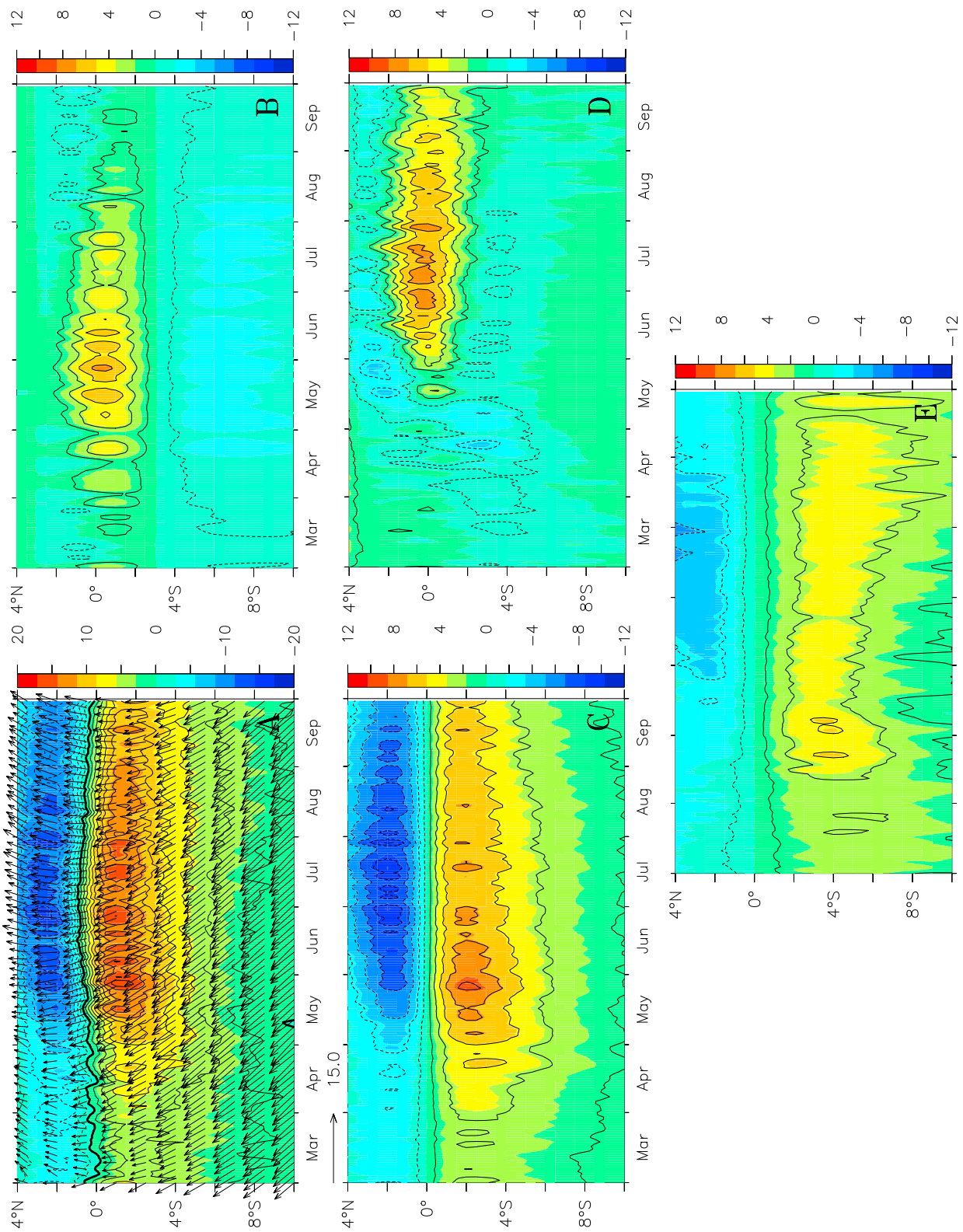

Figure 4

[24] The current velocity in a homogeneous frictional surface layer of constant depth H on a β plane centered on the equator, can be written as [*Zebiak and Cane*, 1987]

$$\begin{cases} ru_s - \beta y v_s = \dfrac{\tau_x}{\rho_0 H} \\ rv_s + \beta y u_s = \dfrac{\tau_y}{\rho_0 H} \end{cases}, \tag{3}$$

where the subscripted s is for the depth-averaged current velocities (u, v); r is a linear damping coefficient, somewhat arbitrarily adjusted (here we adopt (1.5 days)$^{-1}$). The wind stress components are represented by τ_x, τ_y. From these equations, the Ekman transport can be easily determined as well as its divergence, giving the Ekman pumping velocity at depth H

$$w_H = \frac{1}{\rho_0 (r^2 + \beta y^2)} \cdot \left\{ \frac{\beta(\beta^2 y^2 - r^2)}{r^2 + \beta^2 y^2} \tau_x + \frac{-2\beta^2 yr}{r^2 + \beta^2 y^2} \tau_y + r\nabla.\tau + \beta y \nabla \times \tau \right\}. \tag{4}$$

The right hand side of equation (4) is composed, from left to right, of terms proportional to the zonal wind stress, the meridional wind stress, the divergence of the wind stress, and the wind stress curl. Additional discussion of the terms of equation (4) is provided in Appendix A.

[25] The Hovmøller latitude-time diagrams of Figure 4 document the relative contribution of each of the four terms in equation (4) to the seasonal cycle of the pumping. These terms have been computed from European Centre for Medium-Range Weather Forecasts (ECMWF) wind stress (spatial resolution is 0.5°) over a 10 year period (1998–2007) to be representative of a climatological state in the EEA. The same time period is now used for all the parameters analyzed in the rest of this section and sections 2.4, 3.1, and 3.2.

[26] During the warm season, surface winds are generally weak over the EEA, whereas during the cold season they intensify, blowing northwestward in the southern hemisphere and veering northeastward after crossing the equator due to the Coriolis force (Figure 4a). Also in Figure 4a, the absolute value of the Ekman pumping is stronger in the belt 3°S–3°N, with positive values (upwelling) south and negative (downwelling) north of the equator. This allows us to explain the singular position of the ACT, confined in the narrow band south the equator, with a sharp northern boundary locked along the equator. Of the four terms, the largest contribution to Ekman pumping is made by the meridional wind stress term (Figure 4c). In April, the strengthening of the meridional wind stress (Figure 4c) and the wind stress curl (Figure 4e), is such that both contribute to an early increase in Ekman pumping south of the equator. The other two terms, proportional to the zonal component of the wind stress (Figure 4b) and the divergence (Figure 4d) are centered on the equator, a consequence of the values of the coefficient of the zonal wind stress and of the divergence in equation (4), which are even function of the distance to the equator (see Appendix A). These terms further strengthen the positive pumping south of the equator (by a comparable order of magnitude) between May and June. Note also that the divergence term becomes positive in late May (Figure 4d), lagging the zonal (Figure 4b) and meridional (Figure 4c) wind stress terms by 1 and 2 months, respectively. All terms contribute to the rapid cooling of SST during this period. The influence of cross-equatorial winds on equatorial upwelling has already been analyzed with a complex model by *Philander and Pacanowski* [1981b]. Here, it is shown that Ekman theory can also simply explain the bulk of the ACT.

[27] In conclusion, consideration of the Ekman pumping on the equatorial β plane can explain qualitatively the cooling induced at the mixed layer base and at the surface. It allows for the determination of (1) the shape of the ACT confined along the southern side of the equator; (2) its early formation in April, during the intensification of the meridional wind stress component and to a lesser extent of its curl; (3) its persistence into early autumn (although weaker after August); and (4) the robustness of the yearly appearance of the ACT in the EEA, due to the positive contribution of each of the four terms to the Ekman pumping in May–June.

2.4. Equatorial Front and Winds

[28] Figure 5 summarizes the seasonal evolution of the latitudinal structure of zonally averaged SSTs and surface winds. For SSTs, the *Reynolds et al.* [2007] climatology is used and winds are from ECMWF; both are 10 year averages over the period 1998–2007 and monthly mean values averaged over 10°W–4°E (i.e., a zonal averaging domain large enough to represent the extent of the ACT core, see Figure 1; farther east, the ACT is strongly influenced by coastal upwelling, and farther west, tropical instability waves continuously deform the equatorial front).

[29] Large-scale features apparent in Figure 5a include (1) the cooling of SSTs at all the latitudes from April to August; (2) the prolonged existence of global south-to-north positive SST gradients between 10°S and 4°N; (3) the increase of these global 10°S–4°N SST gradients with an increased seasonal cooling between April and September at 10°S compared to 4°N; (4) an indication that the cooling does not occur monotonically with latitude is manifest more strongly between May and July near 2°S in the ACT; and (5) that this cooling induces marked meridional gradients north and to a smaller extent, south of 2°S.

[30] The wind profiles (Figure 5b) exhibit (1) global north-to-south positive gradients between 10°S and 4°N, thus reversed compared to the global 10°S–4°N SST gradients; (2) an overall seasonal wind increase between April and August; (3) weaker winds appear in June near 1°S, migrate southward and are located near 3°S in September;

Figure 4. Hovmøller latitude-time diagrams of the mean (a) total Ekman pumping (10^{-6} m s^{-1}) and vector wind speed (m s^{-1}), (b) pumping due to the zonal component of the wind stress, (c) pumping due to the meridional component of the wind stress, (d) pumping due to the divergence of the wind stress, and (e) pumping due to the wind stress curl. The means have been computed over 1998–2007 from ECMWF surface winds and wind stress and are zonally averaged over 10°W–4°E; pumping units are 10^{-6} m s^{-1}. Note the different scale for Figure 4a versus and Figures 4b–4e. Contour intervals are 2×10^{-6} m s^{-1}.

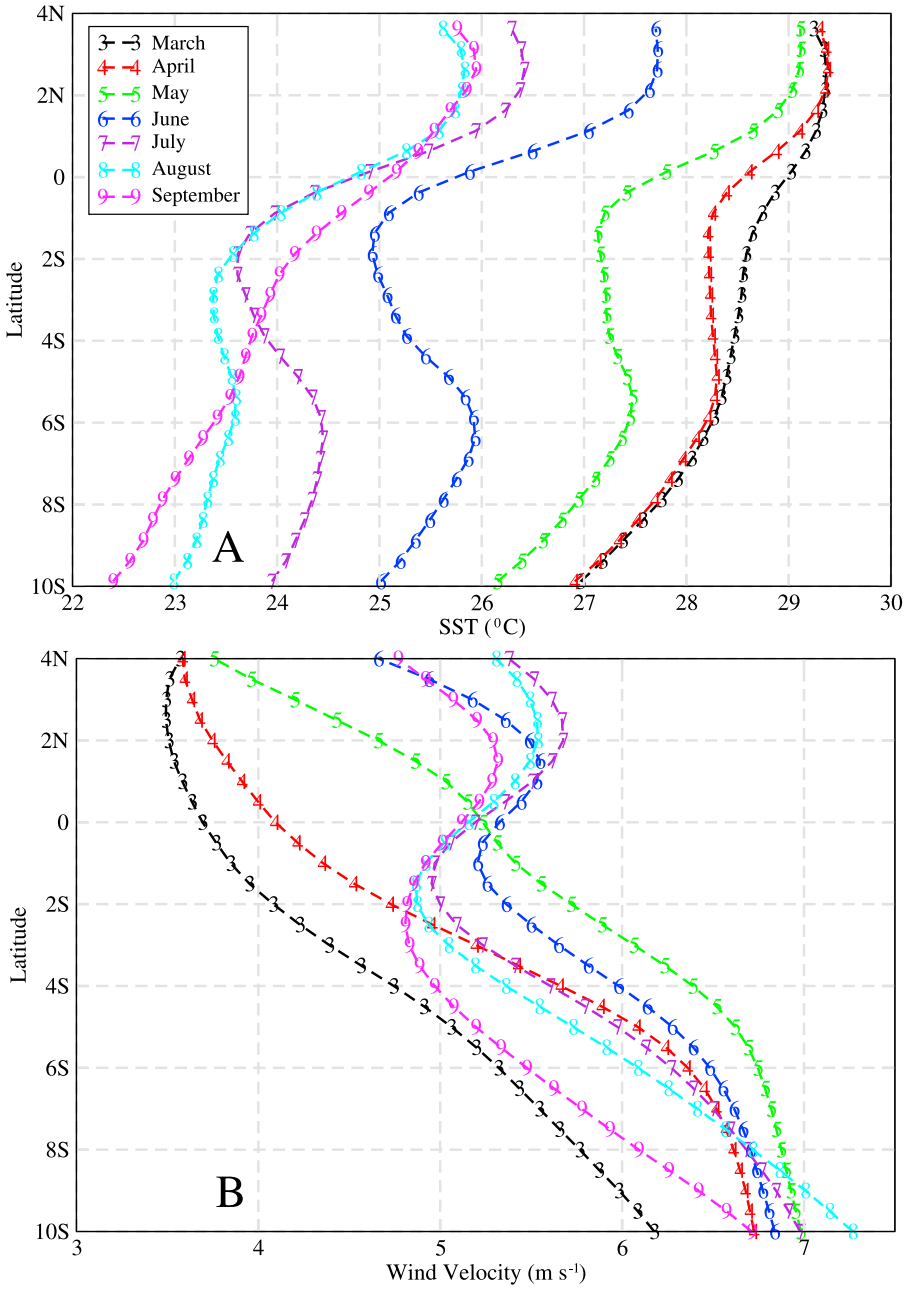

Figure 5. Monthly evolution of the latitudinal distribution of zonally averaged (10°W–4°E): (a) *Reynolds et al.*'s [2007] sea surface temperatures (°C) and (b) ECMWF wind speed magnitude (m s^{-1}). SSTs and winds are averaged over the period 1998–2007.

and (4) an almost concomitant wind maximum present at 2°N from June to September.

[31] The coevolution of SSTs and winds is compared with Hovmøller latitude-time diagrams of zonally averaged (over 10°W–4°E) SSTs and ECMWF winds (Figure 6, as in Figure 5, both variables are time averaged over 1998–2007). Three zones can be identified in Figure 6a: (1) north of the equator (zone A), where SSTs are the warmest and cool gradually from the end of May to the end of July; (2) from the equator to 5°S (zone B), where cooling begins earlier (end of April) and is pronounced until August; this zone corresponds to the ACT; and (3) from 5°S to 10°S (zone C), where SST cooling is slower than in zone B but faster than in zone A. The three zones are delineated by meridional SST gradients; one is located on the equator between zone A and zone B. Here gradients are pronounced, they correspond to the equatorial SST front and increase as soon as April to mid-July and relax in August–September. The other, near 5°S between zone B and zone C, is characterized by weaker meridional gradients (which do not allow for clear identification of an SST front), vanishing in August, when the seasonal cooling of the southern hemispheric SSTs reaches its northernmost extension.

[32] The wind diagram (Figure 6b) clearly captures the seasonal intensification of the southern hemisphere winds that expand northward over the EEA. The northward pro-

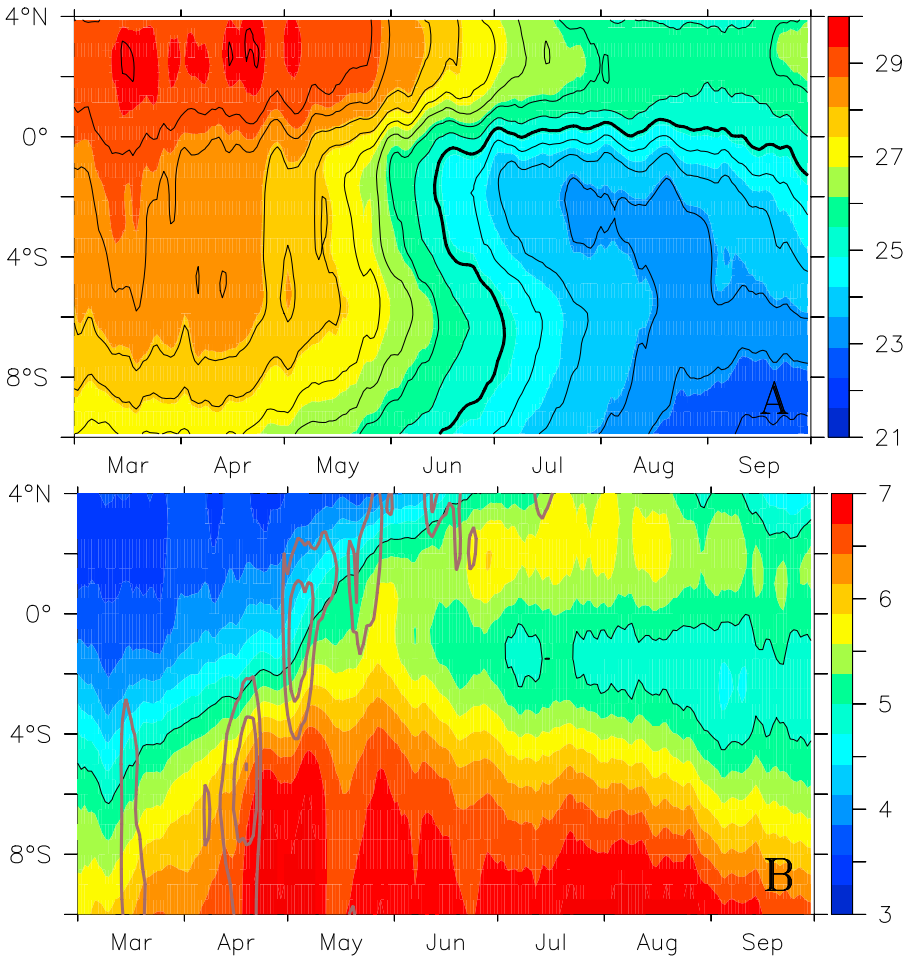

Figure 6. Hovmøller latitude-time diagrams of (a) *Reynolds et al.*'s [2007] sea surface temperatures (°C) (the contour interval is 0.5°C and the 25°C isotherm is represented by the bold black contour) and (b) ECMWF wind speed magnitude (m s^{-1}). A 10 day time-averaged filter has been applied to the winds to filter out the intraseasonal variability. The thick brown line represents the wind tendency (m s^{-1} d^{-1}) above the threshold 0.04 m s^{-1} d^{-1} and the 5 m s^{-1} isotach is drawn as a thin black line. All data are averaged over the period 1998–2007 and zonally averaged over 10°W–4°E.

gression of this intensification nearly corresponds to the position of 5 m s^{-1} isotach: located near 4°S in April, it crosses the equator in May and reaches 4°N in June. More importantly, Figure 6b indicates that during the period of the most intense SST gradients, a deceleration of the winds occurs between the equator and 2°S in June. The area of decelerating winds gradually widens until it spans 0°S–4°S at the end of September. Simultaneously, the winds increase in the northern hemisphere, where they reach their maximum near 2°N from mid-June to the end of August. At the West African coast (4°N), the wind speed reaches its maximum in July and August. Note that the absolute wind speed maximum never occurs north of 2°N. This suggests that this is not the continental circulation that spreads offshore, but, instead, the effect of an oceanic influence on WAM flow. If such a continental forcing was due to the development of the heat low only, then seasonal wind strengthening over the EEA would be akin to a large sea breeze, spreading from the continent toward the ocean. Such a feature is not observed on Figure 6b.

[33] Additional support for this point is provided in Figure 7. It shows the Hovmøller latitude-time diagram of sea level pressure and related latitudinal gradients. It indicates that (1) over the continent (north of 4°N), the north to south pressure gradient decreases with time in the heat low at latitude higher that 15°N; (2) in the southern hemisphere, the pressure field increases from April to July, before decreasing at the end of August; (3) before May, the quasi absence of pressure gradient over the ocean between 5°S and 5°N does not support the idea of a strong link with what occurs over the continent; in the contrary, the meridional pressure gradient quite reverses near 5°N; and (4) this situation continues through June, when the (negative) pressure gradient field over the ocean increases near 2°S, decreases near 2°N and increases again near the African coast. This suggests that the structure of the sea level pressure gradient is the direct consequence of the development of the equatorial front along the equator.

[34] Finally, during the period of the ACT formation, we attribute the strengthening of the southeasterly winds

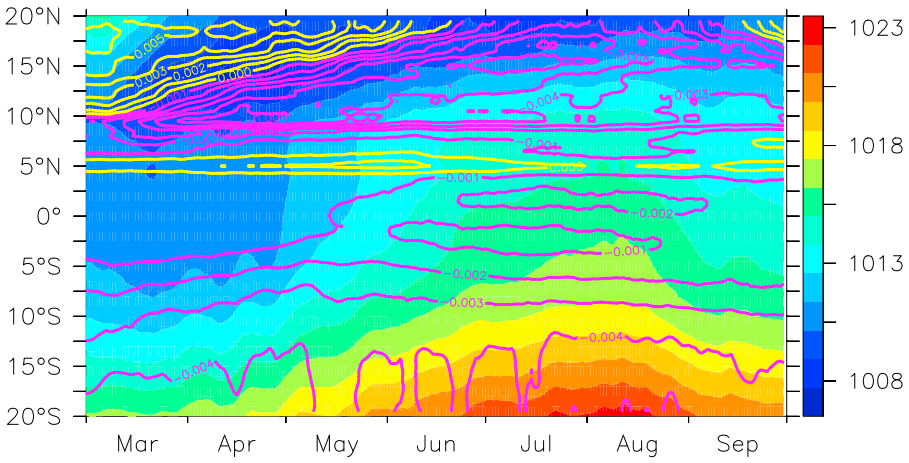

Figure 7. Hovmøller latitude-time diagram of sea level pressure (color, hPa) and meridional sea level pressure gradients (lines, hPa km^{-1}) from ECMWF over the period 1998–2007 and zonally averaged over 10°W–4°E. Yellow (magenta) lines are positive (negative) north-south pressure gradients.

in the southern hemisphere mainly to the dynamic of the St. Helena anticyclone. On the contrary to what happens over the continent where winds are largely driven by the African heat low, over the ocean, winds are mainly driven by what occurs both on the northern side of the St. Helena anticyclone and over the ACT.

3. Relationships Between Atlantic Cold Tongue and Monsoon Onset

3.1. Ocean-Atmosphere Coupling

[35] SST cooling south of the equator develops as soon as the intensification of the southern hemispheric trades reaches the equator. Between the beginning of the SST cooling at the end of April and the appearance of the acceleration (deceleration) north (south) of the equator in mid-June, nearly 1.5 months have elapsed (see Figure 6). This finding strongly supports the existence of a delayed atmosphere-ocean coupling. The large-scale wind pattern is responsible for the formation of the ACT (a passive actor at this stage). Then, approximately 1.5 months later, the ACT serves to accelerate (decelerate) winds in the northern (southern) hemisphere before they enter into and strengthen the WAM flow. Figure 8 represents the 10 year mean north-south SST gradients in a Hovmøller latitude-time diagram. The gradients are positive from March to September in the belt 2°N–2°S, while maxima are reached from May to August. After June, there is a southward shift of the band of maximum SST gradients, from 1°N in June to 1°S in September. Negative SST gradients are present north of 3°N from July to September, collocated with the seasonal upwelling zones along the Ivorian and Ghanaian coasts.

[36] However, the atmosphere does not respond to the SST gradient itself, but to the surface net heat flux (i.e., the sum of the latent heat flux, sensible heat flux, net longwave and net shortwave heat fluxes) gradient. In these components latent heat, sensible heat and the upward longwave heat flux are all largely dependant on SST but not the others. We show below that surface heat flux gradients over the EEA may differ from SST gradients. Hovmøller latitude-time diagrams of net surface heat fluxes and associated meridional gradients (Figure 9) have been computed from the ECMWF operational analyses. ECMWF heat fluxes were selected because, of the NWP models, they validated best against the Analyze Multidisciplinaire de la Mousson Africaine (AMMA) [*Redelsperger et al.*, 2006] data set [*Caniaux et al.*, 2007].

[37] The 10 year mean values averaged over 10°W–4°E are shown in Figure 9. The net heat flux is positive (ocean warming) over the ACT waters and negative (ocean cooling) between 10°S and 4–6°S from mid-April to August (Figure 9a). The extent of this negative net heat flux area recedes south-

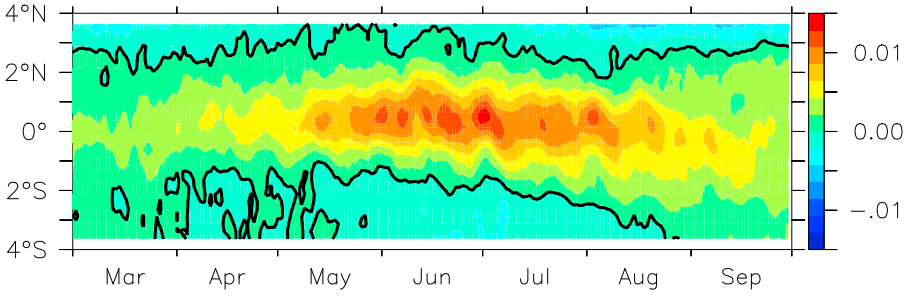

Figure 8. Hovmøller latitude-time diagram of meridional sea surface temperature gradients (°C km^{-1}) from *Reynolds et al.*'s [2007] sea surface temperatures averaged over the period 1998–2007 and zonally averaged over 10°W–4°E. The thick black line is the zero line.

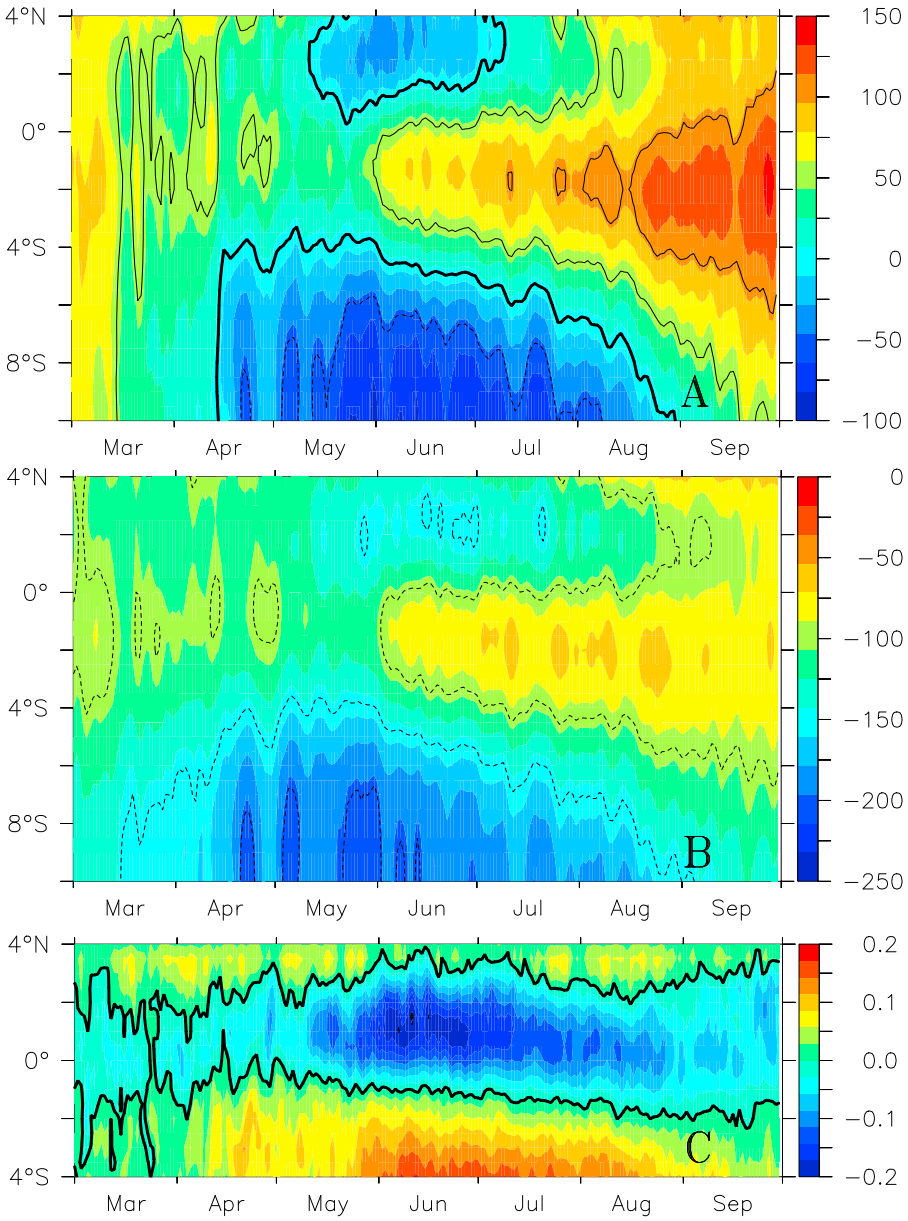

Figure 9. Hovmøller latitude-time diagrams of ECMWF: (a) net surface heat fluxes (W m^{-2}, contour interval is 50 W m^{-2}), (b) sum of the latent heat and sensible heat fluxes (W m^{-2}, contour interval is 50 W m^{-2}), and (c) net surface heat flux gradients (W m^{-2} km^{-1}). Data are averages over the period 1998–2007 and zonally averaged over 10°W–4°E. The thick black line is the zero line.

ward with time as a consequence of the cooling ACT. Another region of negative fluxes is present from mid-May to mid-July north of 2°N up to the African coast. In this area the negative net heat flux is not due to the dominant latent heat flux contribution (as in the region between 10°S and 4–6°S), but to the reduced contribution of the incoming solar radiation which is limited by the extensive cloud cover present in this area (not shown).

[38] The distribution of positive fluxes over the ACT (Figure 9a) appears well associated with the pattern of weaker winds over the ACT (Figure 6b). It implies that the winds are an important factor for increasing the turbulent surface heat fluxes and consequently the net heat flux in this area. The sum of the latent and sensible heat fluxes present a maximum between −100 and −50 W m^{-2} over the ACT compared to the other regions (Figure 9b). As a consequence, a belt of negative sea surface heat flux gradients (Figure 9c) extends from 2°S to 3°N from April to September with maxima centered at 1°N from mid-May to the end of July. Note that there is a good correspondence between the negative heat flux gradients (Figure 9c) and the positive SST gradients (Figure 8), except that heat flux gradients exhibit maxima earlier than SST gradients. We do not attribute this difference to SSTs nor winds, but to the variation in net solar heat flux, which is on average associated with an increase in cloudiness north of the equator, relative to the south.

[39] This is shown in Figure 10, where the maximum meridional SST gradient (Figure 10a) occurs 3 weeks after

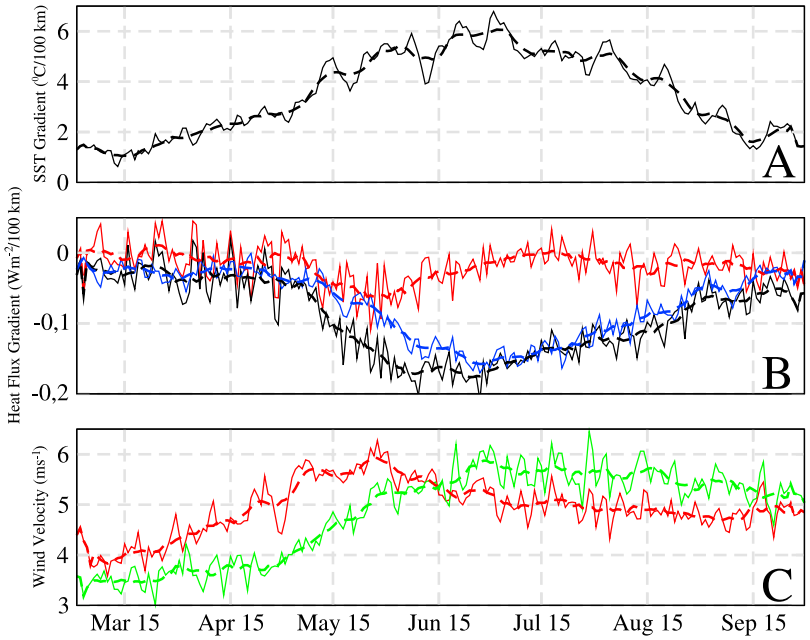

Figure 10. Time evolution of (a) meridional SST gradients (°C/100 km) at 0.5°N; (b) meridional gradients of net surface heat fluxes (black), net solar radiations (red), nonsolar heat flux (blue), sum of latent heat flux, sensible heat flux, and longwave radiation (W m^{-2}/100 km) at 0.5°N; and (c) winds (m s^{-1}) at 2°S (red) and 2°N (green). All curves represent 10 year averages (1998–2007) over 10°W–4°E. Thick dashed curves have been obtained after filtering the series (thin solid lines) with a 10 day running average. SSTs are from *Reynolds et al.* [2007] and winds and heat fluxes are from ECMWF.

the minimum net sea surface heat flux gradients at 0.5°N (Figure 10b). The contribution of the solar radiation to the decrease in net heat flux gradients is greatest from May to June (Figure 10b), when there is persistent cloud cover over the GG. This result points to the nonnegligible role of incident solar radiation to the net heat flux in the EEA. In Figure 10c, the wind strengthening at 2°N coincides with a decrease in the net heat flux gradient at the end of April (Figure 10b). This strengthening lasts until the beginning of July, after which net heat flux gradients start to increase. At 2°S, the decrease in winds takes place later, but still during the period when net heat fluxes decrease.

[40] Finally, in light of the fields presented previously, we suggest the following scenario: in the presence of the ACT, cold (warm) water is associated with high (low) pressure on the southward (northward) side of the equatorial front. As a result of the surface pressure field, centers of divergence (convergence) are positioned over the region of maximum (minimum) heat flux, in a pattern consistent with the mechanisms proposed by *Lindzen and Nigam* [1987] and *Hayes et al.* [1989] or *Wallace et al.* [1989] and recently discussed by *Small et al.* [2005] or *Song et al.* [2006]. When surface wind is driven by pressure gradient force alone and the pressure gradient is proportional to the SST (or heat flux) gradient [e.g., *Lindzen and Nigam*, 1987], wind speed is maximized at the SST front or downstream the SST front in case of southerly winds [*de Szoeke and Bretherton*, 2004] and the center of surface wind convergence (divergence) is located over the cold (warm) SSTs. As the air moves from the cold to warm water, the stability of the lower atmosphere decreases and the enhanced vertical mixing accelerates surface winds over the SST front, resulting in the observed collocation of the SST front and maximum surface wind divergence [e.g., *Hayes et al.*, 1989; *Wallace et al.*, 1989].

[41] A consequence of these mechanisms is that the monsoon wind acceleration in the GG and associated divergence help to reduce atmospheric instability, resulting in the northward migration of moist air and convection toward the African continent, as hypothesized by *Okumura and Xie* [2004] from a modeling study.

3.2. Interannual Variability

[42] If the ACT is to exert an influence on the WAM onset, then an early (late) ACT onset must correspond to an early (late) WAM onset, as suggested for years 2005 and 2006 by *Janicot et al.* [2008]. In this section, we are analyzing whether statistical links can be established between the ACT and WAM onsets. The development of the WAM has been described by *Sultan and Janicot* [2000] as occurring with a "jump." To characterize this jump, the authors derived an index based on satellite precipitation in Hovmøller latitude-time diagrams. Due to the relationship between OLR and convective precipitation, and the relative robustness of OLR retrievals, the precipitation index was based on OLR variations by *Sultan and Janicot* [2003]. Note also that in some studies the monsoon onset is not defined by the northward jump of precipitation over the African continent, but by the southeasterly wind increase over the Gulf of Guinea in April–May. To our knowledge, no WAM onset dates based on this definition exist in the literature.

[43] In this study the WAM onset dates computed by *Fontaine and Louvet* [2006] are used. The authors used an index based on two satellite precipitation data sets: Climate Prediction Center Merged Analysis of Precipitation (CMAP)

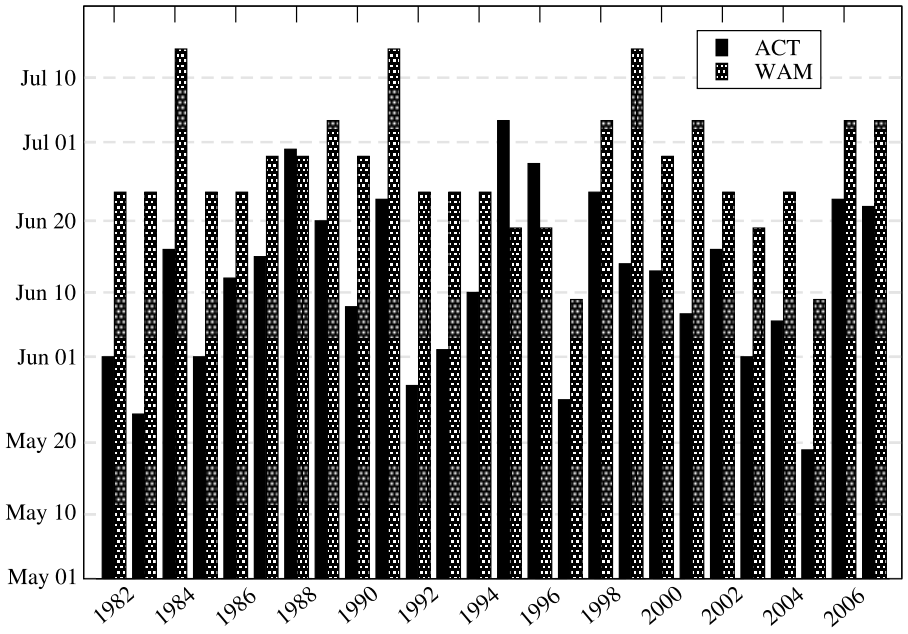

Figure 11. Onset dates for the ACT (black bars) and WAM (gray bars) during the period 1982–2007. For the Atlantic cold tongue, the dates were computed with index T_1 (see text); West African monsoon onset dates are from *Fontaine and Louvet* [2006] obtained with the GPCP precipitation data set.

[*Xie and Arkin*, 1997] and the Global Precipitation Climatology Project (GPCP) [*Adler et al.*, 2003; *Xie et al.*, 2003]. They defined the WAM onset date as the first pentad of a 20 day period registering a positive WAM onset index (i.e., the difference between 10°W–10°E averaged precipitation over the region north of 7.5°N and the region south of 7.5°N) in the both CMAP and GPCP data sets. They provide the dates of the WAM onset by pentad over 1979–2004 and note that the WAM onset can be well defined certain years and less well other years. However, they concluded that, on average, the results obtained with the two precipitation data sets are concordant, and agree well with *Sultan and Janicot*'s [2003] results based on OLR data. In the present study, B. Fontaine (personal communication, 2008) provided us with WAM onset dates up to 2007 by using the same criteria as for the period 1979–2004.

[44] For the ACT, two indices have been considered. The first one aims to capture the onset of the ACT, keeping in mind that once initiated, the extension of this cooling to the southern EEA is quite rapid in April–May. Its definition is based on the first appearance of this cooling, and the date T_1 corresponds to the date at which the surface area of the ACT (as defined in section 2) exceeds 0.40×10^6 km^2. The second index has more direct physical meaning and relies on the intensity of SST gradients at the northern boundary of the ACT. To compute this index, the daily maximum of the SST gradient (∇SSTMax) has been calculated in the belt 4°S–4°N from *Reynolds et al.*'s [2007] SSTs, averaged over the band 10°W–4°E. The index is defined as the excess of a predefined minimum SST gradient ∇SST_0 to express its intensity

$$Index = \sum_d (\nabla SST\mathrm{Max}(d) - \nabla SST_0) H_e(\nabla SST\mathrm{Max}(d) - \nabla SST_0), \quad (5)$$

where H_e is the Heaviside function ($H_e = 1$ when ∇SSTMax $(d) > \nabla SST_0$ and 0 otherwise). The use of ∇SST_0 is to filter the smallest structures resulting from the SST gradient fields; its value has been fixed empirically at 0.006°C km^{-1} after some tests. T_2 is the date at which this index exceeds an empirical threshold fixed at 0.25°C km^{-1}. Note that T_2, the date when significant SST gradients occur, falls after T_1, the date of the ACT onset.

[45] The series of ACT and WAM onset dates are shown in Figure 11. As expected, the WAM onset follows the ACT onset by some weeks, except in 1988, 1995, and 1996. The delay depends on the different thresholds adopted but, as the ACT forms relatively rapidly, a low sensitivity was noted in the correlations. *Fontaine et al.* [2008] noted that for years 1988 and 1995 (and also 1998) the monsoon onset was unclear, i.e., there was neither a sudden shift in time nor an abrupt latitudinal shift of the monsoon, meaning that the "monsoon onset" concept itself cannot be applied for these specific years. For the other years, meridional SST gradients seem to be a discriminating factor in the coupled mechanism involved between the ACT and WAM onsets.

Table 2. Statistics Obtained for the Dates of the Atlantic Cold Tongue with Dates $T_1$and T_2 and West African Monsoon Onsets[a]

	CMAP	GPCP	GPCP With 1988, 1995, 1996, and 1998 Omitted
T_1	0.32 (0.11)	0.49 (0.02)	0.80 (<0.001)
T_2	0.31 (0.12)	0.43 (0.03)	0.64 (<0.001)

[a]Date T_1 is based on its surface area and T_2 is based on SST gradients (see text). Statistics are from *Fontaine and Louvet* [2006] with CMAP and GCPC precipitation data sets. Also shown are statistics that were obtained from GPCP data after omitting years 1988, 1995, 1996, and 1998 in the series (see text). Statistics include the Spearman rank correlation coefficients with corresponding level of significance given in parentheses.

[46] Table 2 presents the statistics obtained when correlating T_1 and T_2 with WAM onset dates computed with either CMAP or GPCP, and in the last column, correlations obtained with GPCP with "unclear" years 1988, 1995, 1996, and 1998 discarded. The Spearman rank correlation coefficients are between 0.31 and 0.80 with levels of significance less than 0.12. The correlations are clearly improved when the WAM onset is established with the GPCP data, and when years of unclear monsoon onset dates and times when the ACT appears after monsoon onset are excluded.

4. Conclusions

[47] Analyses presented in this paper point to strong interactions between the Atlantic cold tongue (ACT) and the wind pattern over the eastern equatorial Atlantic (EEA). The results define the main characteristics of the seasonal cycle and allow us to distinguish two successive phases.

4.1. First Phase From March to mid-June: Formation of the ACT

[48] 1. In the south hemisphere, the southeastern trades intensify from March to April, in phase with the seasonal evolution of the St. Helena anticyclone. This intensification progresses toward the EEA from southwest to northeast in April–May. This northward progression may result from the northward austral winter march of the St. Helena anticyclone and the associated seasonal pressure increase [*Wauthy*, 1983].

[49] 2. Following the intensification of these winds is the formation of the ACT, which extends the area of seasonally cooled SSTs from the southern hemisphere northward, in the band 0°N–4°S (i.e., the equatorial waveguide). A simple model of the Ekman pumping at the equator can reproduce this seasonal cooling to first order. This model enables to understand why (1) the ACT is bounded between the equator and nearly 4°S, and why, associated to the presence of shallower mixed layers, it occupies the eastern part of the equatorial Atlantic basin; (2) the southeastern sector of the trades favors intense positive pumping; and (3) due to the positive contribution of all the terms (zonal, meridional, divergence and curl) to the total pumping, intense cooling occurs in May–June, i.e., more intense than the cooling north of the equator and south of 4°S.

[50] 3. The ACT exhibits large interannual variability, in terms of onset date, horizontal extension, duration and intensity (Table 1), all parameters which exhibit some spread instead of being tightly correlated (Figure 3). Other factors have to be taken in account in order to explain this interannual variability. For instance, enhanced ACT cooling in some years has been statistically related to the Equatorial Undercurrent strengthening by *Hormann and Brandt* [2007], meaning that the oceanic circulation at the whole basin scale can infer on the ACT cooling.

[51] 4. Generally, the ACT appears near 10°W due to the convergence of stronger Ekman pumping associated with early onset intensified trade winds near this location, and more intense mixing by the Equatorial Undercurrent at the base of the mixed layer, as suggested by *Voituriez and Herbland* [1977].

4.2. Second Phase From mid-June to August: Feedback of the ACT Onto the Surface Winds

[52] 1. The presence of the ACT imparts differential SST cooling away from the equator, with more intense and rapid cooling south than north. It thus generates intense cross-equatorial SST gradients (the equatorial front) and surface heat flux gradients. Meridional SST gradients increase on average from March to the end of June before relaxing until mid-September. These gradients assume a narrow belt between 1°N and 1°S, and recede progressively southward. Their longitudinal extension is limited at around 20°W.

[53] 2. Surface heat flux gradients reflect the SST gradient pattern (with opposite sign), except that they are minimal earlier (on average at the beginning of June, instead of the end of June for the SST gradient) due to decreased solar radiation consecutive to increased cloudiness north of the equator during this WAM preonset period.

[54] 3. During the short period when surface heat flux gradients at the northern edge of the ACT are intense enough, a local circulation establishes over the EEA, superimposed over the large-scale circulation of the southeastern trades, which decelerate south of the equator and increase to the north after crossing the equator, with a maximum found near 2°N. Cross-equatorial sea surface heat flux gradients are inferred to cause the northward (southward) propagation of a divergence zone (convergence). The stronger the flux gradients are, the stronger the low-level wind increase (decrease) and divergence (convergence) north (south) of the equator. Certainly, the process by which low-level stability increases in the marine atmospheric boundary layer due to cold SSTs [*Hayes et al.*, 1989; *Wallace et al.*, 1989], contributes to the wind decrease south of the equator.

[55] 4. Strengthening of the winds on the northern side of the equator contributes to the northward migration of low-level moisture and convection, and pushes rainbands to the north.

[56] 5. It can be hypothesized that this temporary strengthening of the low-level circulation can impact the WAM jump, especially when in phase with the Saharan heat low effect. In this regard, the dates of the WAM jump and ACT formation have been shown to be tightly correlated.

[57] We stress that, in addition to the preexisting large-scale circulation, which is composed of the large-scale land-sea pattern that primarily drives the African monsoon system [e.g., *Li and Philander*, 1997; *Biasutti et al.*, 2005], the Hadley circulation which maintains the link between the Saharan heat low and the St. Helena anticyclone [e.g., *Wang*, 2002, 2005], and the large-scale teleconnections of the WAM system with other ocean basins [e.g., *Wang et al.*, 2009; *Fontaine et al.*, 2010], the presence of the ACT induces a secondary local circulation that also sets up at the scale of the eastern equatorial Atlantic during the preonset period. These results confirm that during the second phase, the ACT is an active part of the ACT-WAM coupled system as already suggested by previous studies [e.g., *Vizy and Cook*, 2002; *Gu and Adler*, 2004; *Okumura and Xie*, 2004; *Hagos and Cook*, 2009] and is not only a passive response to the monsoon circulation.

[58] *Okumura and Xie* [2004] in particular provide a conceptual model of the seasonal evolution of the WAM-ACT complex. They argue that the leading process of the

ACT cooling is the acceleration of the southerly winds along the pressure gradient, which results from heating of the West African continent. Moreover, in response to the onset of the WAM, the upwelling cooling is strongest in the EEA because of the strong acceleration of the southerly winds and because the thermocline is shallow there. Our detailed model diverges however from their scheme on three important issues: first, because such a pressure gradient with the African continent is not seen (Figure 7); second, because the ACT cooling is anterior to the onset of the WAM as shown in Figure 11; third, because over the Gulf of Guinea the wind increase is from the ocean toward the continent (Figures 6b and 7), and is mainly a consequence of the St. Helena anticyclone, reinforced by the local wind increase due to the surface heat flux gradients associated with the presence of the equatorial front in the EEA.

[59] It seems very likely that the St. Helena anticyclone is one of the major drivers of interannual variability in the WAM onset, as identified by *Janicot et al.* [2008]. Due to its importance in the timing of the ACT formation, the intensification of the southeastern trade winds in the southern hemisphere and its variability is an important issue which need to be studied further. The St. Helena anticyclone remains one of the less well documented and studied anticyclones. This point is important, since coupled models generally fail to reproduce the correct position and intensity of this anticyclone and this affects the Atlantic basin as a whole [*Seager et al.*, 2003; *Richter et al.*, 2008].

Appendix A

[60] The proportionality coefficients of each term on the right hand side of equation (4) are designed C_1 for the zonal wind stress, C_2 for the meridional wind stress, C_3 for the divergence of the wind stress, and C_4 for the wind stress curl. The variations of the four coefficients with latitude are plotted in Figure A1. C_1 and C_3 are even functions of the distance to the equator y, while C_2 and C_4 are odd functions of y. C_1 and C_3 have extremes positioned just on the equator while the position of C_2 and C_4 extremes depend on r. The smaller the value of r, the closer to the equator and greater the extremes are. For common values of r, the maxima of C_2 and C_4 are located in the belt 3°S–3°N (Figure A1). It follows that the sign and intensity of the Ekman pumping results from (1) asymmetries away from the equator due to the different sign of the coefficients C_1 to C_4 and (2) the relative intensity of the N-S and E-W components of the wind stress. For instance, a northeasterly wind from 45° generates a positive pumping north of the equator and no pumping south of the equator.

[61] From equation (4) and Figure A1, it can be deduced that in absence of wind stress divergence and curl, the Ekman pumping is symmetrical away from the equator, and is positive (negative) and at a maximum (minimum) at the equator for easterly (westerly) winds. Similarly, nondivergent or nonrotational southerly (northerly) winds generate asymmetric pumping away from the equator with positive (negative) and negative (positive) pumping south and north of the equator, respectively. From Table A1 and Figure A2, we can deduce that the orientation of dominant winds in the EEA

Table A1. Sign of the Ekman Pumping Due to the First Two Terms in Equation (4) as Functions of the Sign of Coefficients C_1 and C_2, the Wind Stress (τ_x, τ_y) Sector, and Latitude[a]

	Wind Stress Sector			
	SW	NW	NE	SE
		>3°N		
C_1	ascending	ascending	ascending	ascending
C_2	descending	descending	descending	descending
τ_x	ascending	ascending	descending	descending
τ_y	ascending	descending	descending	ascending
w_H for C_1	ascending	**ascending**	descending	**descending**
w_H for C_2	descending	**ascending**	ascending	**descending**
		0°N–3°N		
C_1	descending	descending	descending	descending
C_2	descending	descending	descending	descending
τ_x	ascending	ascending	descending	descending
τ_y	ascending	descending	descending	ascending
w_H for C_1	**descending**	descending	**ascending**	ascending
w_H for C_2	**descending**	ascending	**ascending**	descending
		3°S–0°N		
C_1	descending	descending	descending	descending
C_2	ascending	ascending	ascending	ascending
τ_x	ascending	ascending	descending	descending
τ_y	ascending	descending	descending	ascending
w_H for C_1	descending	**descending**	ascending	**ascending**
w_H for C_2	ascending	**descending**	descending	**ascending**
		<3°S		
C_1	ascending	ascending	ascending	ascending
C_2	ascending	ascending	ascending	ascending
τ_x	ascending	ascending	descending	descending
τ_y	ascending	descending	descending	ascending
w_H for C_1	**ascending**	ascending	**descending**	descending
w_H for C_2	**ascending**	descending	**descending**	ascending

[a]Words are bold when both coefficients C_1 and C_2 confer the same sign to the pumping.

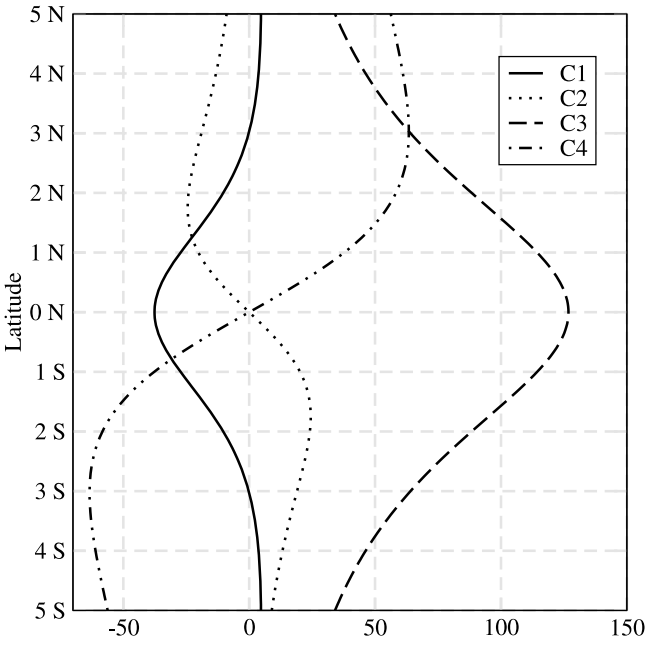

Figure A1. Variations of coefficients C_1 to C_4 in equation (4) with latitude. C_1 and C_2 have been multiplied by 10^5 to be compared to coefficients C_3 and C_4.

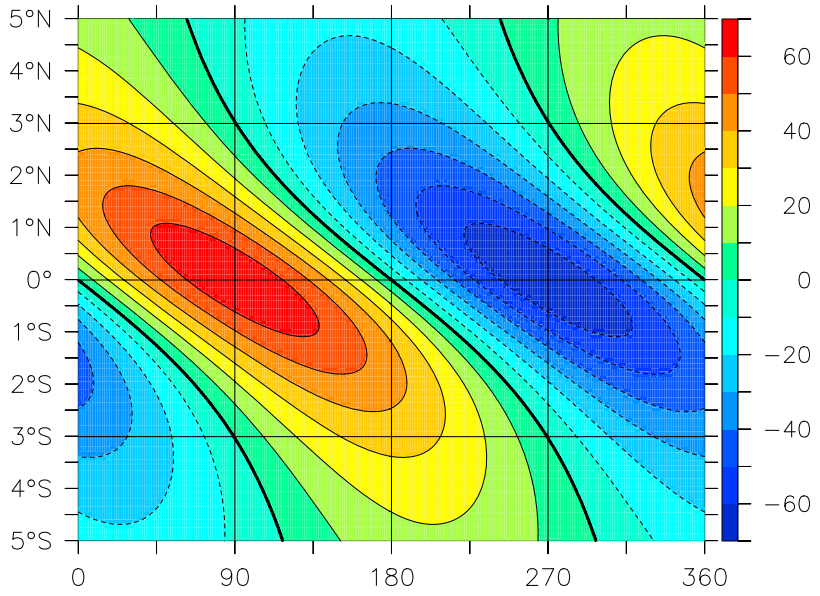

Figure A2. Ekman pumping (10^{-5} m s^{-1}) as a function of the wind stress sector (x axis in degrees, where 0 and 180 mean northerly and southerly winds, respectively) and latitude (y axis) generated by nondivergent and nonrotational wind stress with an arbitrary velocity.

(see Figure 4a) favors positive pumping south of the equator, stronger in the band 3°S–0°N, whereas north of the equator, negative pumping is favored. In the eastern equatorial Atlantic, the sign and intensity of the Ekman pumping ultimately results from a regional wind pattern dominated by the circulation induced by the St. Helena anticyclone in the southern hemisphere. This specific wind pattern leads to (Figure A2) (1) the presence of upwelling/downwelling in the equatorial belt, confined to a distance of roughly two Rossby radii (3°S–3°N); (2) upwelling south of the equator; (3) its absence north of the equator; and (4) the intensification of upwelling in the western equatorial Atlantic, where winds are stronger and gain strength earlier in the season than in the eastern equatorial Atlantic.

[62] **Acknowledgments.** This study was supported by the AMMA project. Based on a French initiative, AMMA was built by an international scientific group and is currently funded by a large number of agencies, including those in France, the United Kingdom, United States, and Africa. It has been the beneficiary of a major financial contribution from the European Community's Sixth Framework Research Programme. Detailed information on scientific coordination and funding is available on the AMMA International Web site http://www.amma-international.org. Special thanks are dedicated to Bernard Fontaine who provided the dates of the WAM onsets and to the National Climatic Data Center for making Reynolds' data available online. We also thank two anonymous reviewers for their useful comments on the manuscript.

References

Adamec, D., and J. J. O'Brien (1978), The seasonal upwelling in the Gulf of Guinea due to remote forcing, *J. Phys. Oceanogr.*, *8*, 1050–1060, doi:10.1175/1520-0485(1978)008<1050:TSUITG>2.0.CO;2.

Adler, R. F., et al. (2003), The version 2 Global Precipitation Climatology Project (GPCP) monthly precipitation analysis (1979–present), *J. Hydrometeorol.*, *4*, 1147–1167, doi:10.1175/1525-7541(2003)004<1147:TVGPCP>2.0.CO;2.

Bakun, A. (1978), Guinea current upwelling, *Nature*, *271*, 147–150, doi:10.1038/271147a0.

Biasutti, M., D. S. Battisti, and E. S. Sarachik (2005), Terrestrial influence on the annual cycle of the Atlantic ITCZ in an AGCM coupled to a slab ocean model, *J. Clim.*, *18*, 211–228, doi:10.1175/JCLI3262.1.

Busalacchi, A. J., and J. Picaut (1983), Seasonal variability from a model of the tropical Atlantic ocean, *J. Phys. Oceanogr.*, *13*, 1564–1588, doi:10.1175/1520-0485(1983)013<1564:SVFAMO>2.0.CO;2.

Caniaux, G., F. Guichard, D. Bourras, E. Key, H. Giordani, and B. Bourlès (2007), Evaluation of sea surface flux fields from NWP models, paper presented at Second International AMMA Conference, Afr. Monsoon and Multidiscip. Anal., Karlruhe, Germany, 26–30 Nov.

Colin, C. (1989), Sur la variabilité dans le Golfe de Guinée: Nouvelles considérations sur les méchanismes d'upwelling, Ph.D. thesis, Mus. Natl. d'Hist. Nat., Paris.

de Szoeke, S. P., and C. S. Bretherton (2004), Quasi-Lagrangian large eddy simulations of cross-equatorial flow in the east Pacific atmospheric boundary layer, *J. Atmos. Sci.*, *61*, 1837–1858, doi:10.1175/1520-0469(2004)061<1837:QLESOC>2.0.CO;2.

Fontaine, B., and S. Louvet (2006), Sudan-Sahel rainfall onset: Definition of an objective index, types of years and experimental hindcasts, *J. Geophys. Res.*, *111*, D20103, doi:10.1029/2005JD007019.

Fontaine, B., S. Louvet, and P. Roucou (2008), Definition and predictability of an OLR-based West African monsoon onset, *Int. J. Climatol.*, *28*, 1787–1798, doi:10.1002/joc.1674.

Fontaine, B., J. Garcia-Serrano, P. Roucou, B. Rodriguez-Fonseca, T. Losada, F. Chauvin, S. Gervois, S. Sijikumar, P. Ruti, and S. Janicot (2010), Impacts of warm and cold situations in the Mediterranean basins on the West African monsoon: Observed connection patterns (1979–2006) and climate simulations, *Clim. Dyn.*, *35*, 95–114, doi:10.1007/s00382-009-0599-3.

Gu, G., and R. F. Adler (2004), Seasonal evolution and variability associated with the West African monsoon system, *J. Clim.*, *17*, 3364–3377, doi:10.1175/1520-0442(2004)017<3364:SEAVAW>2.0.CO;2.

Hagos, S. M., and K. H. Cook (2009), Development of a coupled regional model and its application to the study of interactions between the West African monsoon and the eastern tropical Atlantic ocean, *J. Clim.*, *22*, 2591–2604, doi:10.1175/2008JCLI2466.1.

Hardman-Mountford, N. J., and J. M. McGlade (2003), Seasonal and interannual variability of oceanographic processes in the Gulf of Guinea: An investigation using AVHRR sea surface temperature data, *Int. J. Remote Sens.*, *24*, 3247–3268, doi:10.1080/0143116021000021297.

Hastenrath, S., and P. J. Lamb (1978), On the dynamics and climatology of surface flow over the equatorial oceans, *Tellus*, *30*, 436–448, doi:10.1111/j.2153-3490.1978.tb00859.x.

Hayes, S. P., M. J. McPhaden, and J. M. Wallace (1989), The influence of sea surface temperature on surface wind in the eastern equatorial Pacific: Weekly to monthly variability, *J. Clim.*, *2*, 1500–1506, doi:10.1175/1520-0442(1989)002<1500:TIOSST>2.0.CO;2.

Hisard, P. (1973), Variations saisonnières à l'equateur dans le Golfe de Guinée, *Cah. ORSTOM Ser. Oceanogr.*, *11*, 349–358.

Hormann, V., and P. Brandt (2007), Atlantic equatorial undercurrent and associated cold tongue variability, *J. Geophys. Res.*, *112*, C06017, doi:10.1029/2006JC003931.

Houghton, R. W. (1989), Influence of local and remote wind forcing in the Gulf of Guinea, *J. Geophys. Res.*, *94*, 4816–4828, doi:10.1029/JC094iC04p04816.

Janicot, S., et al. (2008), Large-scale overview of the summer monsoon over West and central Africa during AMMA field experiment in 2006, *Ann. Geophys.*, *26*, 2569–2595, doi:10.5194/angeo-26-2569-2008.

Kolodziejczyk, N., B. Bourlès, F. Marin, J. Grelet, and R. Chuchla (2009), Seasonal variability of the Equatorial Undercurrent at 10°W as inferred from recent in situ observations, *J. Geophys. Res.*, *114*, C06014, doi:10.1029/2008JC004976.

Le Barbé, L., T. Lebel, and D. Tapsoba (2002), Rainfall variability in West Africa during the years 1950–90, *J. Clim.*, *15*, 187–202, doi:10.1175/1520-0442(2002)015<0187:RVIWAD>2.0.CO;2.

Li, T., and S. G. H. Philander (1997), On the seasonal cycle of the equatorial Atlantic Ocean, *J. Clim.*, *10*, 813–817, doi:10.1175/1520-0442(1997)010<0813:OTSCOT>2.0.CO;2.

Lindzen, R. S., and S. Nigam (1987), On the role of sea-surface temperature-gradients in forcing low-level winds and convergence in the tropics, *J. Atmos. Sci.*, *44*, 2418–2436, doi:10.1175/1520-0469(1987)044<2418:OTROSS>2.0.CO;2.

Mazeika, P. A. (1968), Mean monthly sea surface temperatures and zonal anomalies of the tropical Atlantic, *Ser. Atlas Mar. Environ. Folio 16*, Am. Geogr. Soc., New York.

Merle, J., M. Fieux, and P. Hisard (1980), Annual signal and interannual anomalies of sea surface temperature in the eastern equatorial Atlantic Ocean, *Deep Sea Res.*, *26*, 77–101.

Mitchell, T. P., and J. M. Wallace (1992), The annual cycle in equatorial convection and sea, surface temperature, *J. Clim.*, *5*, 1140–1156, doi:10.1175/1520-0442(1992)005<1140:TACIEC>2.0.CO;2.

Okumura, Y., and S. P. Xie (2004), Interaction of the Atlantic equatorial cold tongue and the African monsoon, *J. Clim.*, *17*, 3589–3602, doi:10.1175/1520-0442(2004)017<3589:IOTAEC>2.0.CO;2.

Philander, S. G. H. (1990), *El Niño, La Niña, and Southern Oscillation*, 293 pp., Academic, San Diego, Calif.

Philander, S. G. H., and R. C. Pacanowski (1981a), Response of equatorial oceans to periodic forcing, *J. Geophys. Res.*, *86*, 1903–1916, doi:10.1029/JC086iC03p01903.

Philander, S. G. H., and R. C. Pacanowski (1981b), The oceanic response to cross equatorial winds (with application to coastal upwelling in low latitudes), *Tellus*, *33*, 201–210, doi:10.1111/j.2153-3490.1981.tb01744.x.

Philander, S. G. H., T. Yamagata, and R. C. Pacanowski (1984), Unstable air-sea interaction in the tropics, *J. Atmos. Sci.*, *41*, 604–613, doi:10.1175/1520-0469(1984)041<0604:UASIIT>2.0.CO;2.

Picaut, J. (1983), Propagation of the seasonal upwelling in the eastern equatorial Atlantic, *J. Phys. Oceanogr.*, *13*, 18–37, doi:10.1175/1520-0485(1983)013<0018:POTSUI>2.0.CO;2.

Redelsperger, J. L., et al. (2006), AMMA: Une étude multidisciplinaire de la mousson Ouest-Africaine, *Meteorologie*, *54*, 22–32, doi:10.4267/2042/20098.

Reynolds, R. W., T. M. Smith, C. Liu, D. B. Chelton, K. S. Casey, and M. G. Schlax (2007), Daily high resolution blended analysis for sea surface temperature, *J. Clim.*, *20*, 5473–5496, doi:10.1175/2007JCLI1824.1.

Richter, I., and S. P. Xie (2008), On the origin of equatorial Atlantic biases in coupled general circulation models, *Clim. Dyn.*, *31*, 587–598, doi:10.1007/s00382-008-0364z.

Richter, I., C. R. Mechoso, and A. W. Robertson (2008), What determines the position and intensity of the South Atlantic anticyclone in austral winter?—An AGCM study, *J. Clim.*, *21*, 214–229, doi:10.1175/2007JCLI1802.1.

Seager, R., R. Murtugudde, N. Naik, A. Clement, N. Gordon, and J. Miller (2003), Air-sea interaction and the seasonal cycle of the subtropical anticyclones, *J. Clim.*, *16*, 1948–1966, doi:10.1175/1520-0442(2003)016<1948:AIATSC>2.0.CO;2.

Small, R. J., S. P. Xie, Y. Wang, S. K. Esbensen, and D. Vickers (2005), Numerical simulation of boundary layer structure and cross-equatorial flow in the eastern Pacific, *J. Atmos. Sci.*, *62*, 1812–1830, doi:10.1175/JAS3433.1.

Song, Q., P. Cornillon, and T. Hara (2006), Surface wind response to oceanic fronts, *J. Geophys. Res.*, *111*, C12006, doi:10.1029/2006JC003680.

Stommel, H. (1960), Wind-drift near the equator, *Deep Sea Res.*, *6*, 298–302.

Stramma, L., and F. Schott (1999), The mean flow field of the tropical Atlantic ocean, *Deep Sea Res. Part II*, *46*, 279–303, doi:10.1016/S0967-0645(98)00109-X.

Sultan, B., and S. Janicot (2000), Abrupt shift of the ITCZ over West Africa and intra-seasonal variability, *Geophys. Res. Lett.*, *27*, 3353–3356, doi:10.1029/1999GL011285.

Sultan, B., and S. Janicot (2003), The West African monsoon dynamics. Part II: The "preonset" and "onset" of the summer monsoon, *J. Clim.*, *16*, 3407–3427, doi:10.1175/1520-0442(2003)016<3407:TWAMDP>2.0.CO;2.

Vizy, E. K., and K. H. Cook (2002), Development and application of a mesoscale climate model for the tropics: Influence of sea surface temperature anomalies on the West African monsoon, *J. Geophys. Res.*, *107*(D3), 4023, doi:10.1029/2001JD000686.

Voituriez, B. (1981), The equatorial upwelling in the eastern Atlantic ocean, *Rep. Final Meet. SCOR WG 47*, pp. 229–247, Nova Southeast. Univ. Press, Fort Lauderdale, Fla.

Voituriez, B., and A. Herbland (1977), Etude de la production pélagique de la zone équatoriale de l'Atlantique à 4°W. Partie I: Relations entre la structure hydrologique et la production primaire, *Cah. ORSTOM Ser. Oceanogr.*, *15*, 313–331.

Waliser, D. E., and C. Gautier (1993), A satellite-derived climatology of the ITCZ, *J. Clim.*, *6*, 2162–2174, doi:10.1175/1520-0442(1993)006<2162:ASDCOT>2.0.CO;2.

Wallace, J. M., T. P. Mitchell, and C. Deser (1989), The influence of sea surface temperature on surface wind in the eastern equatorial Pacific: Seasonal and interannual variability, *J. Clim.*, *2*, 1492–1499, doi:10.1175/1520-0442(1989)002<1492:TIOSST>2.0.CO;2.

Wang, C. (2002), Atlantic climate variability and its associated atmospheric circulation cells, *J. Clim.*, *15*, 1516–1536, doi:10.1175/1520-0442(2002)015<1516:ACVAIA>2.0.CO;2.

Wang, C. (2005), ENSO, Atlantic climate variability and the Walker and Hadley circulations, in *The Hadley Circulation: Present, Past and Future*, edited by H. F. Diaz and R. S. Bradley, pp. 173–202, Kluwer Acad., Dordrecht, Netherlands.

Wang, C., F. Kucharski, R. Barimalala, and A. Bracco (2009), Teleconnections of the tropical Atlantic to the tropical Indian and Pacific oceans: A review of recent findings, *Meteorol. Z.*, *18*, 445–454, doi:10.1127/0941-2948/2009/0394.

Wauthy, B. (1983), Introduction à la climatologie du Golfe de Guinée, *Oceanogr. Trop.*, *18*, 103–138.

Weingartner, T. J., and R. H. Weisberg (1991), On the annual cycle of equatorial upwelling in the central Atlantic Ocean, *J. Phys. Oceanogr.*, *21*, 68–82, doi:10.1175/1520-0485(1991)021<0068:OTACOE>2.0.CO;2.

Xie, P., and P. A. Arkin (1997), Global precipitation: A 17-year monthly analysis based on gauge observations, satellite estimates, and numerical model outputs, *Bull. Am. Meteorol. Soc.*, *78*, 2539–2558, doi:10.1175/1520-0477(1997)078<2539:GPAYMA>2.0.CO;2.

Xie, P., J. E. Janowiak, P. A. Arkin, R. F. Adler, A. Gruber, R. Ferraro, G. J. Huffman, and S. Curtis (2003), GPCP pentad precipitation analyses: An experimental dataset based on gauge observations and satellite estimates, *J. Clim.*, *16*, 2197–2214, doi:10.1175/2769.1.

Zebiak, S. E., and M. A. Cane (1987), A model El Niño–Southern Oscillation, *Mon. Weather Rev.*, *115*, 2262–2278, doi:10.1175/1520-0493(1987)115<2262:AMENO>2.0.CO;2.

G. Caniaux, H. Giordani, F. Guichard, J.-L. Redelsperger, and M. Wade, CNRM-GAME, Météo-France, CNRS, URA 1357, 42. Ave. G. Coriolis, F-31057 Toulouse, France. (caniaux@meteo.fr)

E. Key, LDEO, Columbia University, PO Box 1000, 3 Marine Biology, 61 Route 9W, Palisades, NY 10964-8000, USA.